

## Design issues of Rotational Single Sheet Tester for Fe-Based Nanocrystalline Alloys at High Frequencies

Long Chen<sup>1,2,3</sup>, Han Xiong<sup>1</sup>, Tong Ben<sup>1\*</sup>, and Shifeng Li<sup>1,3</sup>

<sup>1</sup>Hubei Provincial Engineering Technology Research Center for Power Transmission Line,  
China Three Gorges University, Yichang 443002, Hubei, China

<sup>2</sup>College of Electrical Engineering and New Energy, China Three Gorges University, Yichang 443002, Hubei, China

<sup>3</sup>Yichang Key Laboratory of Information Physics Fusion Defense and Control System, China Three Gorges University,  
Yichang 443002, China

(Received 13 February 2021, Received in final form 2 May 2021, Accepted 4 May 2021)

Measuring the vector magnetic properties of nanocrystalline soft magnetic materials at high frequencies is of great significance to the optimal design and energy saving of the electrical equipment. In this paper, some key design issues are discussed for a rotational single sheet tester (RSST) to further studied the Two-Dimensional (2D) magnetic properties of nanocrystalline alloys in the kilohertz range. Firstly, the magnetization uniformity of the testing sample is analyzed and discussed considering the stray field. Secondly, the magnetizer's geometric dimensions are optimized to achieve higher magnetic flux density levels with the minimum energy consumption. Thirdly, the magnetic field and the magnetic flux density sensing system are optimally designed to measure the nanocrystalline alloys' magnetic properties at high frequencies. Finally, a robust controlling algorithm is developed to control the magnetic flux density waveform to sinusoidal in the  $x$  and the  $y$ -direction. Obtained results show that the proposed structure can measure the vector magnetic properties of nanocrystalline alloys up to 10 kHz.

**Keywords :** Finite element analysis (FEM), nanocrystalline alloys, vector magnetic properties, optimization

### 1. Introduction

The energy consumption reduction of electrical equipment is one of the most critical topics in the modern power grid. Motors and transformers are the leading distributed energy consuming equipment, which directly affecting the entire grid's operating efficiency [1-3]. At the state of the art, the energy consumption in the power system is mainly concentrated in the motor and its drive system, accounting for about 45 % of the total energy consumed in the world every year. This part of electric energy consumption is emitted in carbon dioxide, emitting about 6000 megatons per year and increasing at 100 megatons per year. Therefore, it is very important to increase electric energy utilization efficiency [4-6]. As new kinds of soft magnetic materials, Fe-based nanocrystalline alloys with higher magnetic permeability and higher magnetic flux saturation density compared to ferrites have

excellent application prospects in the field of high-frequency energy conservation [7-9]. In the modern High-Voltage Direct Current (HVDC) transmission system, the nanocrystalline alloys are very promising to be the core materials of the large capacity high-frequency (HF) transformer in the DC-DC converter [10]. So, the detailed magnetic hysteresis properties of such materials should be fully examined in one-dimensional (1D) and two-dimensional (2D) magnetization conditions for the sake of developing highly efficient HF transformers and electrical machines. The IEC 60404-6 mainly used in the 1D magnetic property measurement cannot reflect any information on the material's anisotropy. However, the 2D magnetic properties of nanocrystalline are seldom studied. Under the 2D magnetization conditions, the nanocrystalline alloys' vector magnetic hysteresis properties and anisotropic properties can be thoroughly investigated, which would have significantly value on engineers and scientists [11, 12].

The measurement of 2D magnetic properties for soft magnetic materials has been studied for many decades

©The Korean Magnetism Society. All rights reserved.

\*Corresponding author: Tel: +86-13820296113

Fax: +86-0717-6392173, e-mail: woshibttya@163.com

[13, 14]. The mainly 2D magnetic properties test methods are divided by the specimen shape. The Round Rotational Single Sheet Tester (RRSST) with circular test sample is proved to have good control ability of standard circular loci of the vector  $\mathbf{B}$ . Simultaneously, it would cause more magnetomotive force (MMF) to magnetize the sample due to the large air gap [15]. Smaller air gaps between the specimen and the magnetizer reduce the magnetization energy and the stray field [16]. The Square Rotational Single Sheet Tester (SRSST) with smaller airgaps is proved to have good uniformity in the  $20\text{ mm} \times 20\text{ mm}$  area of the sample and have good reproductivity [17]. As the nanocrystalline/amorphous alloys are extremely thin and brittle after the annealing process, it is very hard to measure the 2D magnetic properties by the RSSTs. In 2011, the 2D magnetic properties of Fe–Si–B Amorphous material were first measured and published by Masato Enokizono [18, 19]. Amorphous alloys with ten stacked layer structures are used in the measuring system. However, this method cannot be directly used in measuring the 2D magnetic properties of nanocrystalline alloys due to their brittleness after the annealing process. In this paper, especially designed Double C Rotational Single Sheet Testers (Double C-RSST) with the square sample, is developed, achieving the minimum MMF consumption in high-frequency magnetization. By considering the influence of the stray field of the tester's magnetizing poles, the uniformity area of the magnetic flux density in the sample is improved to almost the entire sample. To determine the magnetizer's final size, the genetic algorithm (GA) is used to optimize the magnetizing performance of the tester.

Finally, the magnetic flux density waveforms are controlled to sinusoidal by a time-domain PI control algorithm developed in the LabVIEW environment.

## 2. Magnetization Uniformity Considering the Stray Field

The magnetization uniformity of the testing sample is the primary consideration in designing the rotational single sheet tester's magnetizing structure. To the minimum the MMF consumption in the high-frequency magnetization, the air gap  $g$  between the sample and the magnetizing poles should be minimized with acceptable tolerance.

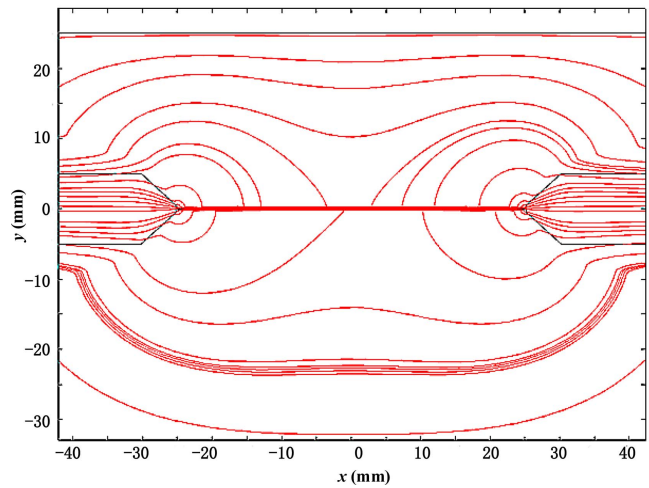


**Fig. 2.** (Color online) The magnetic flux lines around the magnetizing poles and the testing sample in the SRSST.

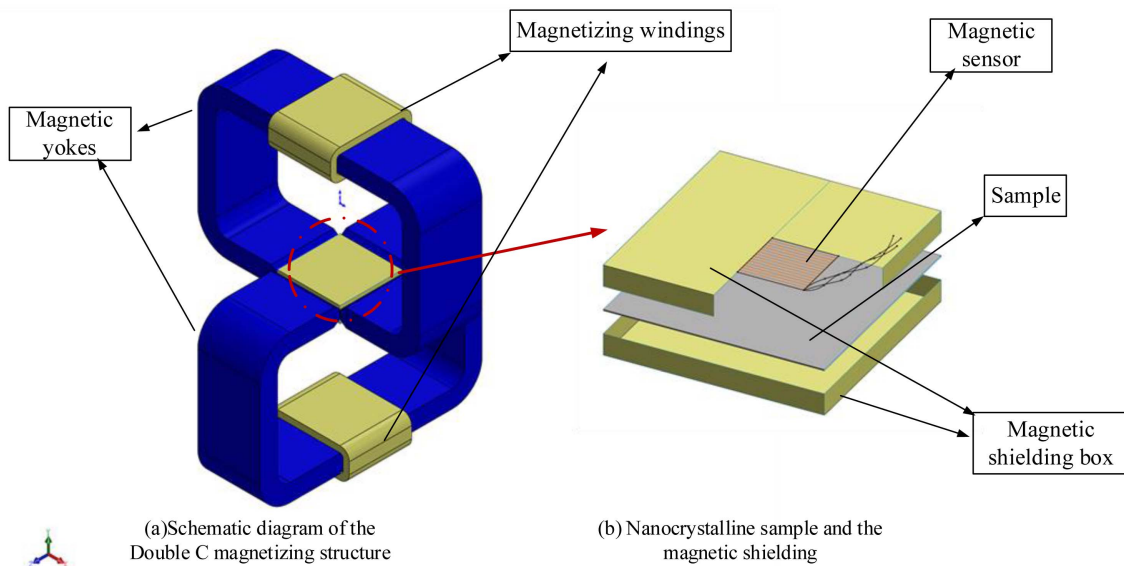
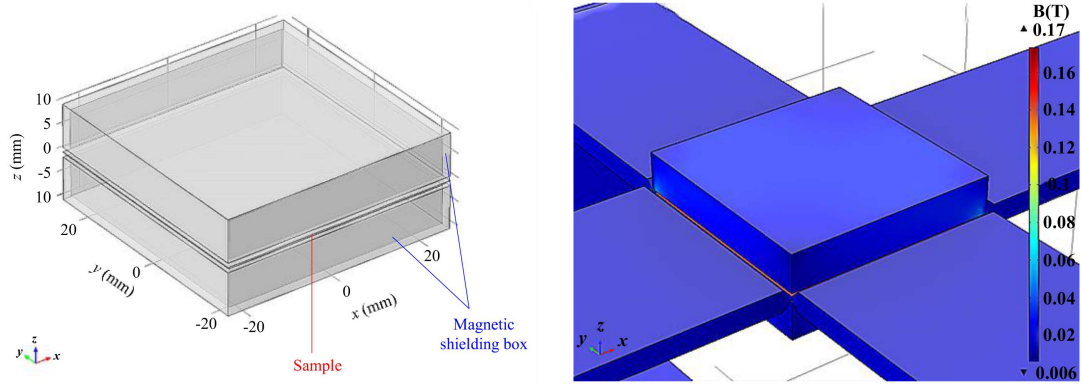


**Fig. 1.** (Color online) The diagram of the double C magnetizing structure and the testing sample of nanocrystalline alloy.

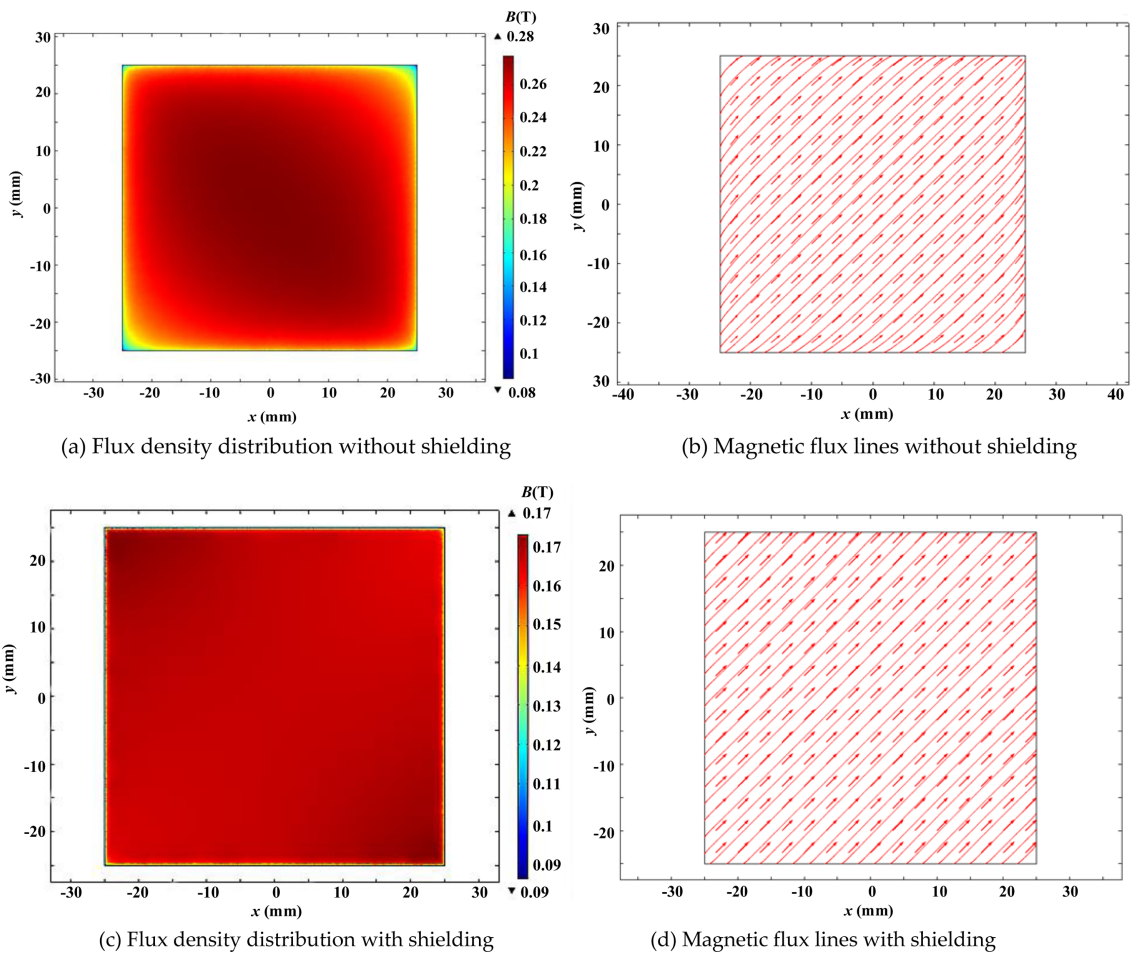


(a) Relative position of the sample and shielding boxes (b) magnetic flux density distribution of the shielding boxes

**Fig. 3.** (Color online) Schematic diagram of the magnetic shielding box.

With the minimal air gap, the round shape sample with the induction motor structure magnetizer is not appropriate because the cogging effect would largely deduce the sample's uniformity area [20]. So, the square sample with

a double C magnetizing yoke structure is proposed in this paper. As the nanocrystalline strip's width is generally less than 50 mm, and the testing sample is cut into 50 mm × 50 mm. The schematic diagram of the proposed mag-



(a) Flux density distribution without shielding

(b) Magnetic flux lines without shielding

(c) Flux density distribution with shielding

(d) Magnetic flux lines with shielding

**Fig. 4.** (Color online) Magnetic flux density distribution and magnetic flux lines in the testing sample with and without the magnetic shielding boxes.

netizing structure is shown in Fig. 1.

In a previous study, the magnetization uniformity is usually analyzed by 2D FEM calculation, which cannot consider the stray field's influence by the magnetizing poles. As shown in Fig. 2, the stray field can largely influence the sample's homogeneous area, and a magnetic shielding technology should be considered. In this paper, a new shielding box structure, shown in Fig. 3, is proposed to protect the sample from the stray field. The 3D FEM calculation has been made to confirm the efficiency of the magnetic shielding box, and the basic magnetization curve has been used in the calculation process.

Calculation results of the magnetic flux density distribution and flux lines distribution in the  $xoy$  plane is shown in Fig. 4. As the  $45^\circ$  is the hardest magnetization direction in the SRSST, the magnetic flux density analysis is realized when the vector magnetic flux density arrows rotate to the  $45^\circ$ . When there is no magnetic shielding box on the sample, the magnetization uniformity of the magnetic flux densities is influenced mainly by the magnetic poles' stray field. The magnetic flux density levels on the corner of the sample are mainly reduced because the stray field of the four magnetizing poles concentrates in the center of the sample. On the contrary, the magnetic shielding box prevents the stray field from the poles to the center of the sample, which led to a relatively uniform flux density distribution.

### 3. Magnetic Circuit Analysis and Optimization of the Double C-RSST

#### 3.1. Magnetic circuit analysis and the design of the exciting windings

The excitation power at high frequencies is the second important factor to be considered in designing the SRSST. The optimization goal of developing the SRSST is to magnetize the square-cut nanocrystalline sample to 1.0 T at a frequency up to 10 kHz. The power amplifier used in this project has a 5.5 kVA capacity, which maximum voltage and current peak values are 150 V and 40 A. To solve the heating problem of the magnetic core for magnetization at high frequency, the magnetic yoke material of the “double C” structure is FT-3M nanocrystalline alloy. The magnetic circuit method combined with frequency-domain FEM calculation is applied to a detailed

analysis of the magnetizer's excitation performance of the SRSST. The specially designed SRSST in this paper, shown in Fig. 1, has a relatively independent magnetic circuit, and we can calculate the parameters separately. According to Ampere's law, the magnetomotive force (MMF) of the  $y$  axial component can be calculated as:

$$F = N_s I = \Phi(R_{sm} + R_{ym} + 2R_{gm}) \quad (1)$$

Where the  $R_{sm}$ ,  $R_{ym}$ ,  $R_{gm}$  are the magnetoresistance of the sample, yoke and the airgap.  $\Phi$  is the magnetic flux in the yoke and the sample. The voltage on the exciting winding without considering flux leakage can be estimated by:

$$u_{coil} \approx 4.44 f N A_{yoke} B_{yoke} = 4.44 f N A_{sa} B_{sa} \quad (2)$$

Where  $N$  is the number of turns of the exciting winding,  $A_{yoke}$  and  $A_{sa}$  are the cross-sectional area of the core and the sample respectively,  $B_{yoke}$  and  $B_{sa}$  are the magnetic flux density in the core and the sample, respectively.

From the magnetic circuit analysis and 3D frequency-domain FEM calculation, it can be obtained that when the MMF  $F = 160$  A, the magnetic flux density in the square sample  $B_{sa}$  is about 1T. Based on the Magnetic circuit analysis above, the number of exciting winding turns can be calculated with the design constraints of current density under  $4 \text{ A/mm}^2$ :

$$N_s = F I_{max}^{-1} \quad (3)$$

Where the  $I_{max}$  is the maximum current calculate from the maximum current density and the Sectional area of winding. To reduce the high-frequency proximity effect and skin effect of the excitation winding, Litz wires are applied to the winding design. The wire diameter of a single conductor can be calculated as:

$$r = \sqrt{2\rho_{Cu}(2\pi\mu_0 f_{max})^{-1}} \quad (4)$$

Where  $\rho_{Cu}$  is the resistivity of copper,  $\mu_0$  is the permeability in a vacuum, and  $f_{max}$  is the highest magnetizing frequency. The final parameters of the exciting windings are shown in Table 1:

#### 3.2. Optimization of the geometric dimensions of the magnetizing structure

The shape of the tester's magnetizing poles has played an important role in optimizing the excitation power of the whole system. Sphenoid-shaped magnetic pole has

**Table 1.** Parameters of the exciting winding at 10 kHz.

Symbol	$N_s$	$D$ (mm <sup>2</sup> )	$N_c$	$R_{ac}$ ( $\Omega$ )	$L$ (mH)
Definition	Number of turns	Conductor diameter	Conductor number of single Litz line	AC resistance	Inductance
Value	12	0.01	300	0.3	0.116

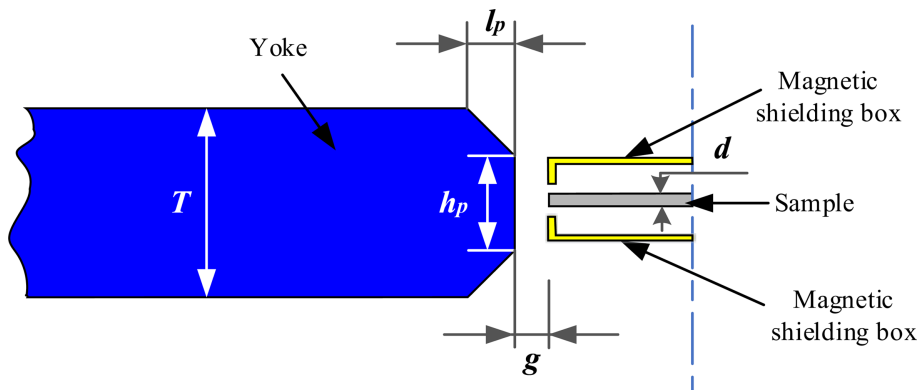


Fig. 5. (Color online) Design variables of the magnetizing structure and the sample.

been proved to have a better magnetic concentration effect [21], while the geometric parameter described in Fig. 5 need to be further investigated by the modern artificial intelligence algorithm. In the optimizing process, some parameters are set to fixed values: The square nanocrystalline sample is cut into 50 mm × 50 mm, where the magnetic flux density and the magnetic field strength are measured. The air gap  $g$ , between the sample and the magnetizing pole, is a crucial parameter influencing the magnetizing performance. A smaller air gap results in a smaller demagnetizing field and less MMF consumption. But the considering the mechanical tolerances, the width of the air gap cannot be infinitely small, which is set to 0.2 mm.

To find the yoke's optimal value, the relationship between the excitation power and yoke thickness is calculated through the FEM calculation. The scanned parameter  $T/d$  is the ratio between the yoke thickness  $T$  and the thickness of sample  $d$  (10 pieces stacked), shown in Fig. 5. Fig. 6(a) shows the variations of MMF  $N_s \times I_p$  and the induced voltage per turn  $e_{coil}/n_s$  required to reach

a rotating peak flux density  $B_p = 1.0$  T in the sample versus the ratio  $T/d$ . The apparent power shown in Fig. 6 (b) is proportional to the product of the  $N_s \times I_p$  and  $e_{coil}/n_s$ . It can be found that the apparent power is minimum when  $T/d$  is about 70, corresponding to the  $T = 14$  mm.

To further determine the shape and size of the Sphenoid magnetizing pole, a GA optimization algorithm has been used in this problem. The optimization goal of this problem can be given as:

$$\min S = u_{coil}(X) \cdot I_{coil}(X) \tag{5}$$

Where the  $S$  is the apparent power required for magnetizing the nanocrystalline sample. The  $u_{coil}$  and the  $I_{coil}$  are the induced voltage and magnetizing current of the excitation coil. The design variables  $X = [x_1, x_2, x_3] = [T, h_p, l_p]$ , which demonstrated in Fig. 5, is the thickness of the yoke, length, and width of the pole.

In the optimizing process, all the design variables are constrained by geometric dimensions and the wedge angle  $\theta$  of the pole, keeping in  $0^\circ \sim 90^\circ$ . By giving the initial value  $X = [16, 5, 6]$  mm, the first optimization point

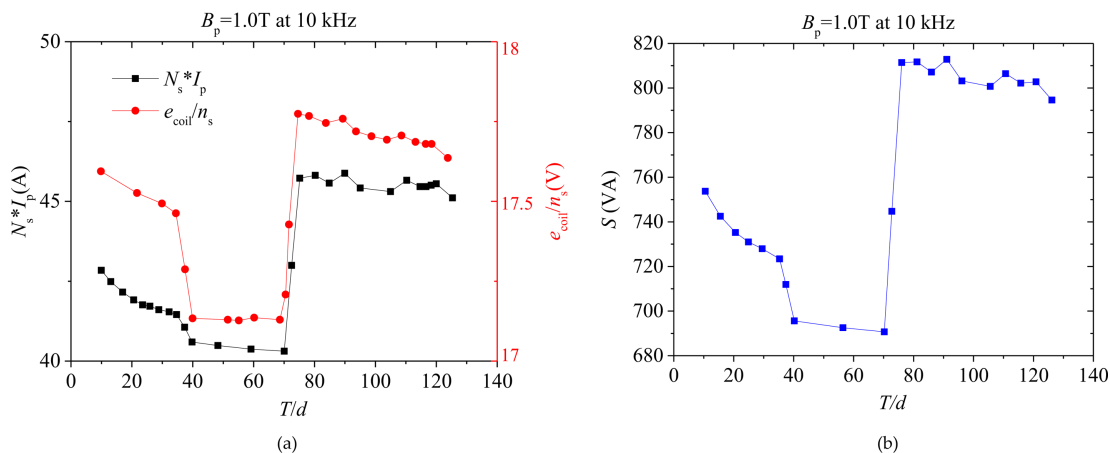
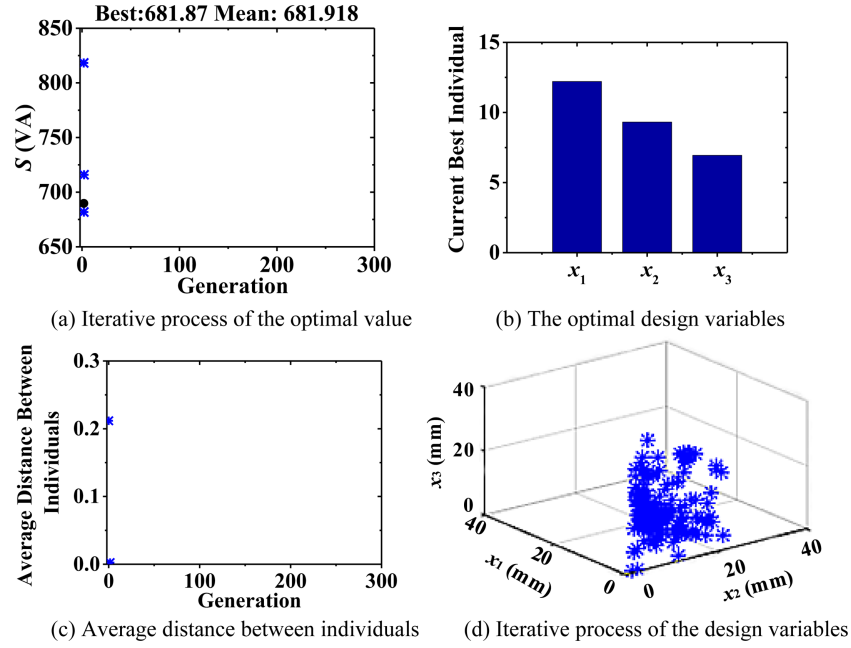


Fig. 6. (Color online) Excitation performance variation with the yoke thickness  $T$ : (a) The MMF and resulting induced potential per turn as a function of  $T/d$ , (b) The apparent excitation power as a function of  $T/d$ .



**Fig. 7.** (Color online) Geometric dimensions optimization process by GA algorithm.

**Table 2.** The initial and the optimal size of the magnetizing pole at 10 kHz.

	$x_1$ (mm)	$x_2$ (mm)	$x_3$ (mm)	S (V·A)
Initial	16	5	6	811
Optimal	13	9	7	681.87

is calculated by the frequency domain FEM calculation. Next, the GA algorithm adjusted the design variables to produce new points in the feasible region space. Finally, after a series of iterations, the optimal solution is satisfied. The iterative process and the final optimization results are shown in Fig. 7. After the optimization process, it is found that the optimal results of the apparent power for magnetizing the sample to 1.0 T is 681.87 V·A, corresponding to the best  $X$  is [13, 9, 7] mm. The excitation performance of the initial and the optimal size of the magnetizing pole are summarized and compared in Table 2.

#### 4. Measuring Principle and Designing of the Vector B-H Sensing Structure

By applying the magnetic fields, which are orthogonal both in space and in time-phasing, the nanocrystalline sample can be magnetized with a rotating magnetic field at any angle in space. As shown in Fig.8, at any instant, the vector magnetic flux density  $\mathbf{B}$  and the vector magnetic field strength  $\mathbf{H}$  in the sample can be expressed as:

$$\mathbf{B}(t) = B_x \sin(\omega t + \phi_B) \mathbf{i} + B_y \cos(\omega t + \phi_B - \frac{\pi}{2}) \mathbf{j} \quad (6)$$

$$\mathbf{H}(t) = H_x \sin(\omega t + \phi_H) \mathbf{i} + H_y \cos(\omega t + \phi_H - \frac{\pi}{2}) \mathbf{j} \quad (7)$$

Where the  $B_x, B_y, H_x, H_y$  are the  $x$  components and the  $y$  components of the vector magnetic flux density  $\mathbf{B}$  and the magnetic field strength  $\mathbf{H}$ .

By applying the Poynting theorem, the power loss per unit mass can be calculated as:

$$P = \frac{1}{T\rho} \int_0^T [\mathbf{H}(t) \cdot \frac{d\mathbf{B}(t)}{dt}] dt \quad (8)$$

Where  $T$  is the period, and  $\rho$  is the mass density.

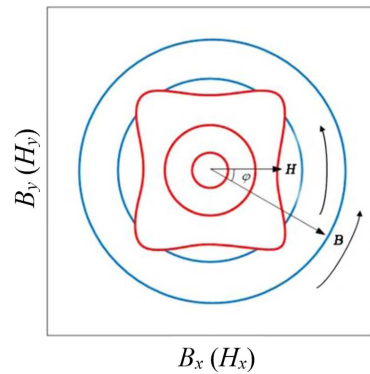


**Fig. 8.** (Color online) The relationship of the vector magnetic flux density  $\mathbf{B}$  and magnetic field strength  $\mathbf{H}$  under rotational magnetization.

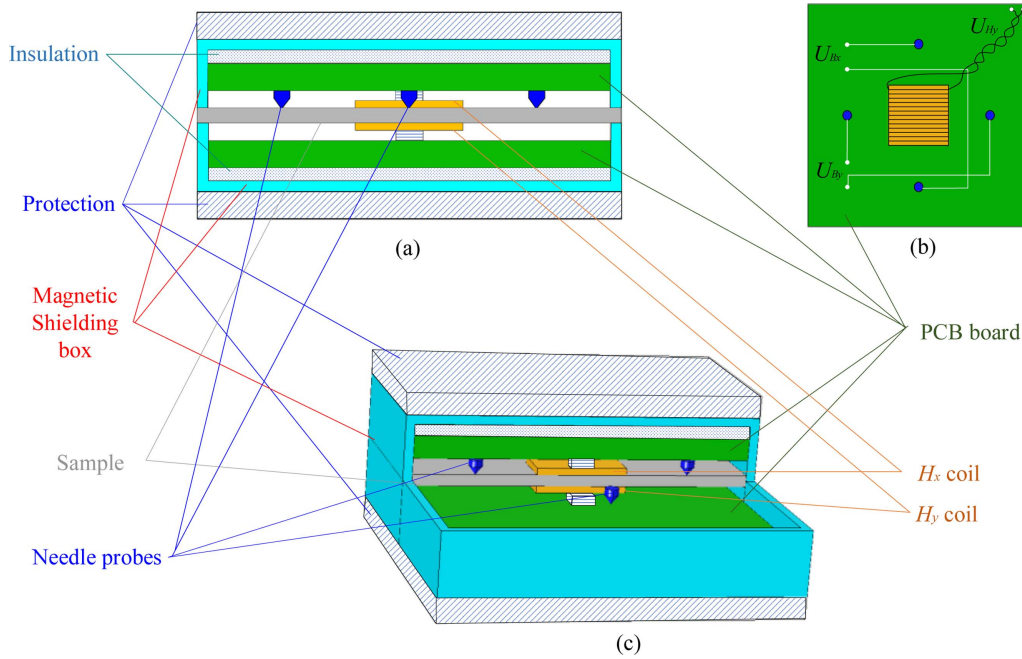


**Fig. 9.** (Color online) Diagram of the vector B-H sensing structure.

To accurately measure the four components in the nanocrystalline sample, a particular designed B-H sensing structure is developed. As shown in Fig. 9, the compact vector B-H sensing structure consists of four parts: 1, Two pairs of needle probes are placed orthogonally to measure the  $x$ , and  $y$  components of the vector magnetic flux density. 2, Two H-coils are closely attached to the sample's upper and lower surfaces to detect the magnetic field strength in the  $x$  and the  $y$ -direction. 3, The magnetic shielding boxes with protections are set around the sample to prevent the external magnetic field's interference from the magnetizing poles. 4, Special designed signal acquisition circuit based on the PCB board and twisted lead structure is used improve the signal acquisition stability. 5, High quality shielded BNC cable is connected to the signal conditioning circuit to prevent signal distortion effectively.

During the measurement of magnetic flux density, the needle probe technique (NPT) is used. The magnetic flux density in the sample is proportional to the induced voltage between the two needle probes demonstrated in Fig. 10(a) [22]:

$$e \approx \frac{1}{2} \int_{S_A} \left( \frac{\partial B}{\partial t} \right) dS = -\frac{1}{2} S_A \frac{dB}{dt} \quad (9)$$

Where the  $S_A$  is the area between probes in the sample. The  $x$  or the  $y$  components of the magnetic flux density can be calculated by:

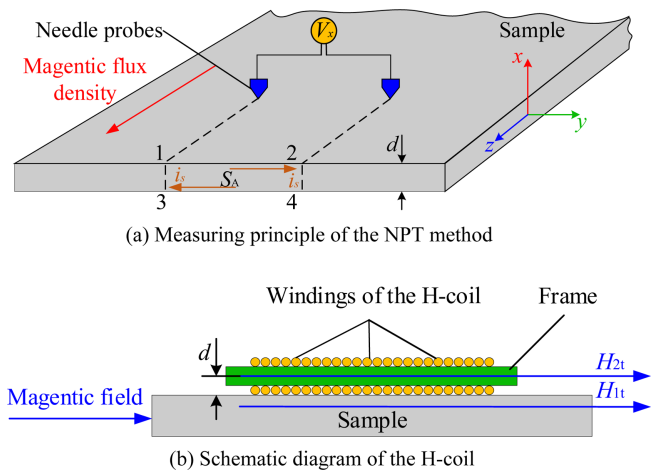
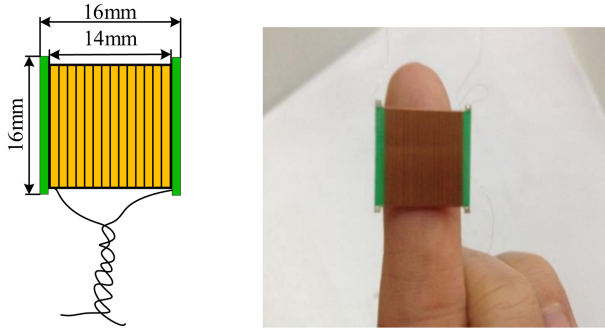


**Fig. 10.** (Color online) The measurement principle of the NPT method for measuring the magnetic flux density and H-coil method for measuring the magnetic field strength.

$$B_i = -\frac{2}{S} \int e_i dt = K_B \int e_i dt \quad (10)$$

Where  $B_i$  and  $e_i$  are the  $i$  ( $i = x$  or  $y$ ) components of the vector magnetic flux density  $\mathbf{B}$  and the corresponding induced voltage. The parameter  $K_B$  is the sensing coefficient of B probes, which can be obtained by measuring the distance between two probes. To get enough single strength, the distance between the needles is set to 30 mm, and the signal resolution of the probe is 4.3 mV/T at 1 kHz.



(a) Dimension parameters of H-coil (b) Photograph of the H-coil  
**Fig. 11.** (Color online) Parameters and photograph of the H-coil.

The  $x$  or  $y$  components of the vector magnetic field strength  $\mathbf{H}$  in the sample can be measured employing the H-coil method, which is based on the principle of tangential continuity of magnetic field on the surface of the sample:

$$H_{1t} = H_{2t} \quad (11)$$

Where  $H_{1t}$  and  $H_{2t}$  are the magnetic field strength in the sample and on the surface of the sample. According to Faraday's law, the  $i$  ( $i = x$  or  $y$ ) components of the magnetic field strength shown in Fig. 10(b) can be calculated by:

$$H_i = -\frac{1}{\mu_0 N_H S_H} \int V_H dt = K_H \int V_{Hi} dt \quad (12)$$

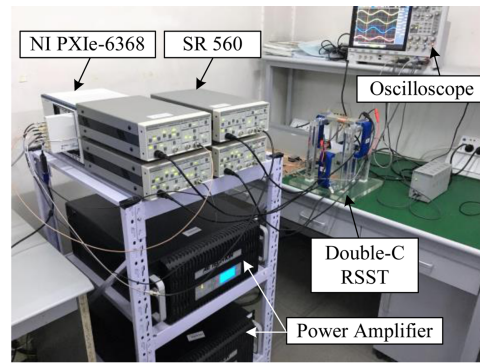
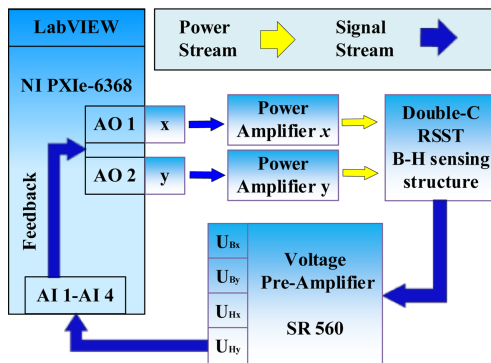
Where the  $N_H$  and  $S_H$  are the numbers of turns and equivalent cross-section of the H-coil, the  $V_{Hi}$  is the induced voltage measured by the H-coil. Because the coil's cross-sectional area is exceedingly difficult to measure, the coefficient  $K_H$  can be calibrated by the standard magnetic field generated by a Helmholtz coil. Considering the H-coil's physical processing difficulty and the area of uniform magnetization in the sample, the

final size of the H-coil is designed as 14 mm × 14 mm × 0.5 mm, as shown in Fig. 11. The corresponding magnetic field measurement resolution can achieve 30 μV/(A/m) at 1 kHz, which is very small and should be further amplified.

### 5. High-frequency Magnetic Properties Measurement System with Feedback Control

The high-frequency vector magnetic properties measurement system for nanocrystalline alloys based on the Double C-RSST is shown in Fig. 12. To realize online measurement and control, NI LabVIEW is applied in the process of signal acquisition. Firstly, the desired waveforms of the excitation voltage are fed in the power amplifier to produce the magnetizing current. Secondly, through the Double C-RSST designed above, the alternating or rotating magnetic field is generated in the square sample. Finally, the vector magnetic flux density  $\mathbf{B}$  and magnetic field strength  $\mathbf{H}$  are detected by the vector B-H sensing structure. As the signals of the induced voltage of the probe and the H-coil are very small, voltage preamplifiers SR560 are used to adjust the signal strength to the level that can be acquired by the NI DAQ card PXI-6115.

Because of the magnetic material's nonlinearity, the measured magnetic flux density in each direction cannot keep sinusoidal when the material began to saturate. A robust control algorithm need to be developed to compensate the magnetic field for producing the standard sinusoidal waveform of the magnetic flux density  $\mathbf{B}$ . Fig. 13 shows the schematic diagram of the periodic point by point sampling control method combing with the PI control theory. In the algorithm, the signals of the four-input analog input (AI) channels of PXI-6115 are pre-conditioning by averaged the data several times to improve



(a) Schematic diagram of measurement and control system (b) Photograph of the measurement system

**Fig. 12.** (Color online) High-frequency vector magnetic properties measurement system.

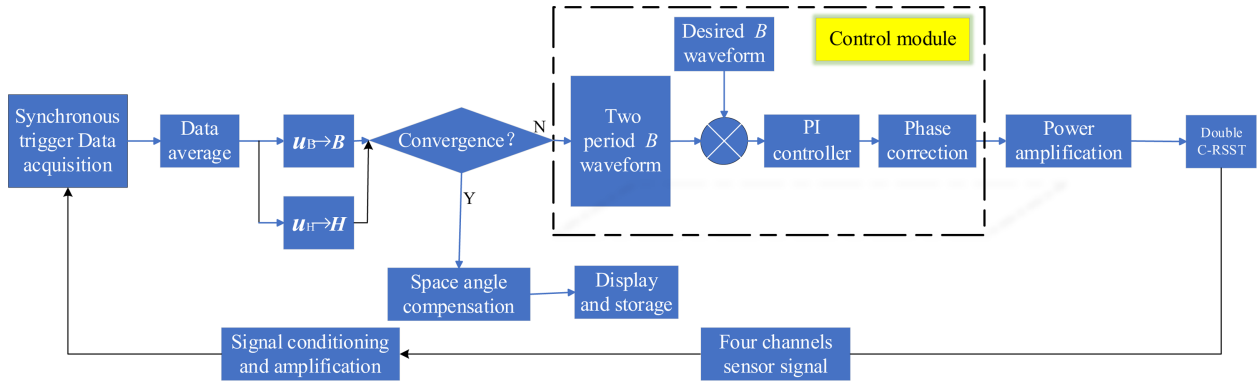
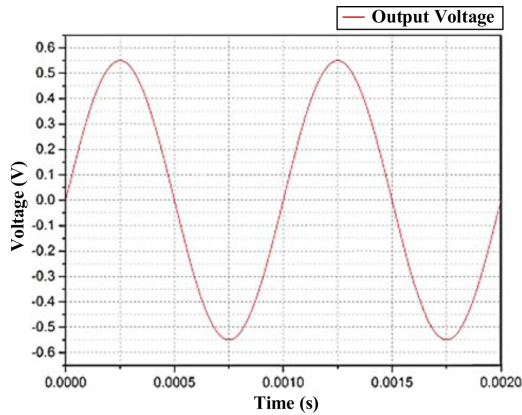


Fig. 13. (Color online) Schematic diagram of Feedback control process.

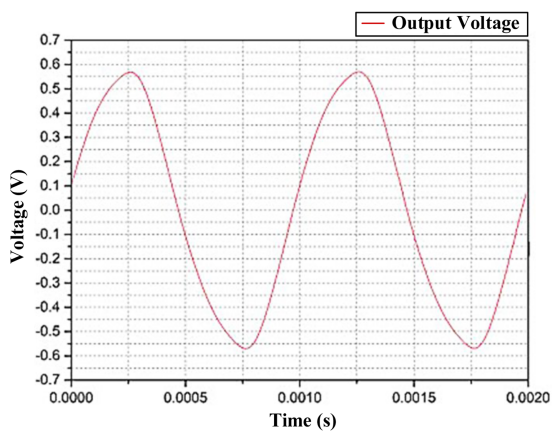
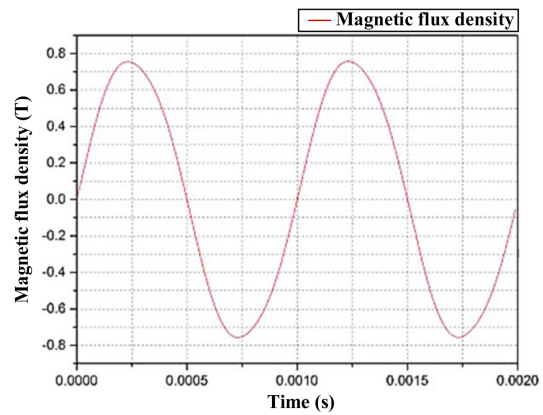
the stability of the data. Then, using the coefficient  $K_B$  and  $K_H$ , the vector B-H sensing structure's induced voltage is converted to the value of the magnetic flux density and the magnetic field strength. Next, two-period flux density waveform points are sent to the control module to calculate the desired output voltage waveform. The output of the controller can be written as:

$$E(n+1) = E(n) + \left( K_p + K_i T + \frac{K_d}{T} \right) (B_i - B_n) - \left( K_p + \frac{2K_p}{T} \right) (B_{ideal} - B_{n-1}) \quad (13)$$

Where the  $E(n)$  represents the output voltage of the nth iteration,  $B_{ideal}$  is the ideal flux density, which is the



(a) The waveform of the output voltage and magnetic flux density before control ( $B=0.8$  T)



(b) The waveform of the output voltage and magnetic flux density after control ( $B=0.8$  T)

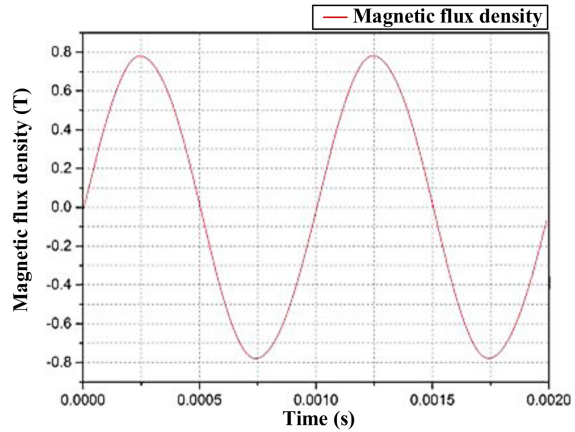


Fig. 14. (Color online) Control performance of the algorithm at  $B=0.8$  T.

standard sinusoidal waveform.  $B_n$ ,  $B_{n-1}$ , and  $B_{n-2}$  represent the flux density waveform in each iteration, respectively.  $K_p$ ,  $K_i$ , and  $T$  represent the proportional, integral coefficient, and sampling period, respectively. The feedback iteration process stopped when the flux density meets the following conditions:

$$\begin{cases} \varepsilon_{FF} = \frac{K_F - 1.11}{1.11} \leq 0.02 \\ \varepsilon_B = \frac{B_{\text{get}} - B_{\text{ideal}}}{B_{\text{ideal}}} \leq 0.02 \end{cases} \quad (14)$$

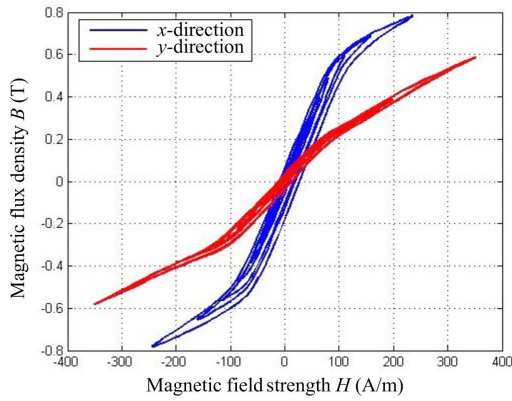
Where the  $K_F$  is the waveform coefficient, which is 1.11 when the waveform is standard sinusoidal.  $\varepsilon_{FF}$  and  $\varepsilon_B$  are the errors of waveform coefficient and flux density amplitude, respectively.

Figure 14 compared the waveform of magnetic flux density with and without the control. It can be found that after applying the feedback controller, the distortion of the waveform is largely reduced, and both the error of

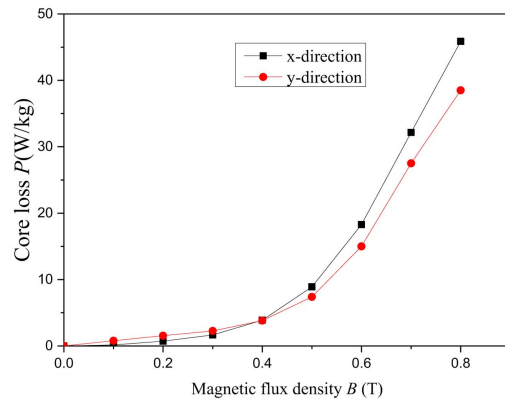
waveform coefficient and flux density amplitude is less than 2 %, which can prove the effectiveness of the proposed method is verified.

## 6. Results and Discussions

The magnetic properties of FeSiBCuNb (FINEMET-type) nanocrystalline alloys up to 10 kHz are measured by the measuring system designed in this paper. As nanocrystalline alloys are fragile due to their brittleness after annealing, the tested sample is pre-loaded into the sensing structure after cutting into 50 mm × 50 mm square. The hysteresis loops and losses under  $x$ -direction (casting direction) and  $y$ -direction (transverse direction) at 10 kHz are measured and shown in Fig. 15. In the  $x$ -direction, the nanocrystalline alloy has higher permeability and higher magnetic density under the same magnetic field strength  $H$ . However, when the flux density level is lower than 0.3 T, the loss in the  $y$ -direction is a little larger than that in the  $x$ -direction while the magnetic density  $B$  is larger than

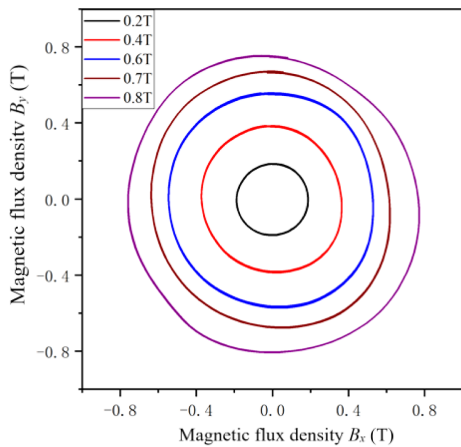


(a) Hysteresis loops in the  $x$  and  $y$  direction

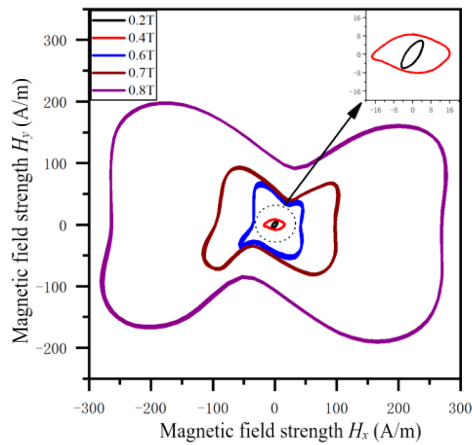


(b) Losses in the  $x$  and  $y$ -direction

**Fig. 15.** (Color online) Hysteresis loops and losses of the nanocrystalline sample magnetized at 10 kHz.



(a) Rotating loci of magnetic flux density



(b) Rotating loci of magnetic field strength

**Fig. 16.** (Color online) Magnetic anisotropy of nanocrystalline alloy under rotational magnetization.

0.4 T, the losses in the  $x$ -direction are higher than that in the  $y$ -direction which is mainly because the main influence factor of loss in lower flux densities is the permeability. In contrast, when the flux density is higher, the lag angle  $\varphi_{BH}$  between the flux density  $B$  and the magnetic field strength  $H$  will become a major contribution to the loss of the material.

To further investigate the anisotropy of the material, the nanocrystalline sample is magnetized by a rotating magnetic field. The loci of the vector magnetic flux density  $B$  are control to circular, and the relationship between the  $B$  loci and  $H$  loci are presented in Fig. 16. The magnetic anisotropy of nanocrystalline alloy is similar to the properties of non-oriented silicon steel under rotating magnetization. However, compared with traditional silicon steel materials, the nanocrystalline alloys' magnetic anisotropy will change when the magnetic flux density increases, and the easy magnetization direction change from casting direction to transverse direction, which is still no good physical explanation for this phenomenon.

## 7. Conclusion

In this paper, optimal design issues of rotational single sheet tester for Fe-Based nanocrystalline alloys at high frequency are analyzed and discussed. Firstly, the magnetizing uniformity considering the stray magnetic field is simulated and analyzed by the FEM method. The uniformity of the sample's magnetic flux density distribution is much improved by proposing the magnetic shielding box structure. Secondly, a specially designed double-C RSST is developed, and the GA algorithm is used in optimizing the excitation performance. Thirdly, a 2D high-frequency magnetic properties measurement system is built based on the special designed vector sensing structure and periodic point by point sampling control method. Based on this system, the magnetic properties of FeSiBCuNb (FINEMET-type) nanocrystalline alloy under alternating and rotating magnetization are measured and analyzed. It is found that the nanocrystalline exist a specific anisotropy and changes with the increase of magnetic flux density. Obtained results are essential both in the energy-saving design of high-frequency transformers and fundamental research in related areas.

## Acknowledgment

This work was supported by the National Natural Science Foundation of China (Grant No. 52007102), the open

foundation of Hubei Provincial Engineering Technology Research Center for Power Transmission Line (2019KXL10), the open foundation of the Yichang Key Laboratory of Information Physics Fusion Defense and Control System, China Three Gorges University (2020XXRH05).

## References

- [1] H. Zhao, C. Ragusa, C. Appino, O. de la Barriere, Y. Wang, and F. Fiorillo, *IEEE Trans. Power Electron.* **3**, 34 (2019).
- [2] Y. Li, B. Wang, and W. Huang, *J. Magn.* **1**, 25 (2020).
- [3] D. H. Kim, B. C. Li, C. H. Song, and K. C. Kim, *J. Magn.* **3**, 25 (2020).
- [4] Y. Li, L. Cao, C. Zhang, Q. Yang, and E. Li, *IEEE Trans. Ind. Appl.* **4**, 26 (2016).
- [5] D. M. Ionel, M. Popescu, M. I. McGilp, T. J. E. Miller, S. J. Dellinger, and R. J. Heideman, *IEEE Trans. Ind. Appl.* **6**, 43 (2007).
- [6] Y. Cuo, J. Zhu, J. Zhong, H. Lu, and J. Jin, *IEEE Trans. Magn.* **2**, 44 (2008).
- [7] Swieboda C. 2011 3rd International Students Conference on, 6-8 Oct 2011, pp. 151-154.
- [8] W. Shen, F. Wang, D. Borovevich, and T. C. Tipton, *IEEE Trans. Ind. Appl.* **1**, 44 (2008).
- [9] A. Makino, T. Kubota, K. Yubuta, A. Inoue, A. Urata, H. Matsumoto, and S. Yoshida, *J. Appl. Phys.* **7**, 109 (2011).
- [10] F. Alves, C. Ramiarinjaona, S. Berenguer, R. Lebourgeois, and T. Waeckerle, *IEEE Trans. Magn.* **5**, 38 (2002).
- [11] L. Chen, Y. Wang, Z. Zhao, H. Zhao, and C. Liu, *AIP Adv.* **5**, 7 (2017).
- [12] V. Valchev, A. Van den Bossche, and P. Sergeant, *J. Magn. Magn. Mater.* **1-2**, 320 (2008).
- [13] X. Ding, S. Ren, Y. Xiong, F. Chen, and J. Xu, *IEEE Trans. Magn.* **10**, 53 (2017).
- [14] Sievert J. *Przegl. Elektr.* **9**, 87 (2011).
- [15] J. Wanjiku and P. Pillay, *IEEE Trans. Ind.* **5**, 51 (2015).
- [16] B. Olivier de la, C. Appino, and F. Fiorillo, *Int. J. Appl. Electrom.* **2**, 48 (2015).
- [17] Y. Kai, S. Zeze, T. Todaka, and M. Enokizono, *IEEE Trans. Magn.* **5**, 49 (2013).
- [18] S. Ueno, T. Todaka, and M. Enokizono, *IEEE Trans. Magn.* **10**, 47 (2011).
- [19] S. Ueno, T. Todaka, and M. Enokizono, *J. Magn. Magn. Mater.* **7**, 111 (2012).
- [20] Y. Li, Q. Zhao, L. Wang, C. Zhang, and R. Yan, *IEEE Trans. Magn.* **11**, 53 (2017).
- [21] Y. Li, Q. Yang, J. Zhu, Z. Zhao, X. Liu, and C. Zhang, *IEEE Trans. Magn.* **2**, 50 (2014).
- [22] Y. Hashimoto, M. Enokizono, and H. Mogi, *J. Appl. Phys.* **10**, 91 (2002).